

Electron-Doping Induced Semiconductor to Metal Transitions in ZrSe₂ Layers via Copper Atomic Intercalation

Zahir Muhammad¹, Kejun Mu¹, Haifeng Lv², Chuanqiang Wu¹, Zia ur Rehman¹, Muhammad Habib¹, Zhe Sun^{1,}, Xiaojun Wu² and Li Song^{1,*}*

¹National Synchrotron Radiation Laboratory, CAS Center for Excellence in Nanoscience, CAS Key Laboratory of Strongly-coupled Quantum Matter Physics, University of Science and Technology of China, Hefei, Anhui, 230029, China.

²CAS Key Laboratory of Materials for Energy Conservation, Synergetic Innovation Centre of Quantum Information & Quantum Physics, CAS Center for Excellence in Nanoscience, and Department of Material Science and Engineering, University of Science and Technology of China, Hefei, Anhui 230026, China.

KEYWORDS: Layered Materials, Phase Transition, Angle Resolved Photoemission Spectroscopy, Electron Doping

ABSTRACT: Atomic intercalation in two dimensional (2D) layered materials can engineer the electronic structure at the atomic scale, bringing out tunable physical and chemical properties which are quite distinct in comparison with pristine one. Among them, electron-doped engineering induced by intercalation is an efficient route to modulate electronic states in 2D layers. Herein, we demonstrate a semiconducting to the metallic phase transition in zirconium diselenide (ZrSe_2) single crystal via controllable incorporation of copper (Cu) atoms. Combined with first-principles density functional theory (DFT) calculations, our angle resolved photoemission spectroscopy (ARPES) characterizations clearly revealed the emergence of conduction band dispersion at M/L point of Brillouin zone due to Cu-induced electron doping in ZrSe_2 interlayers. Moreover, the field-effect transistor (FET) fabricated on ZrSe_2 displayed a n-type semiconducting transport behavior, while the Cu-intercalated ZrSe_2 posed linear I_{ds} vs V_{ds} curves with metallic character shows n-type doping. The atomic intercalation approach has high potential for realizing transparent electron-doping systems for many specific 2D-based electronics.

Layered transition metal dichalcogenides (TMDCs) MX_2 ($\text{M} = \text{Mo}, \text{W}, \text{Zr}, \text{Hf}; \text{X} = \text{S}, \text{Se}$) semiconductors have captivated widespread interest due to their significant superior physical and electrical properties.¹⁻⁶ The crystalline forms of 2D materials have been the subject of intense investigation owing to their unique physical properties⁷, such as direct electronic bandgap in the single-layer limit⁸⁻¹², valence band (VB) splitting¹²⁻¹⁶, valley degree of freedom¹⁷⁻²¹, and excitonic nature of optical band spectra²²⁻²⁶. Artem *et al.* recently observed the, the co-occurrence of exchange splitting and giant SOC in graphene at the same time with good magnetic characteristics²⁷. Thus, TMDCs are considered as an ideal materials for p-n junctions²⁸, field-effect transistors with high mobility of electrons²⁹⁻³¹, memory and switching devices³², optoelectronics and photovoltaic applications³³. These layered materials can also be found in different forms of hybrid or in heterostructure forms.³⁴⁻³⁷ Particularly, the atomic phase engineering can result in observation of tremendous novel physical and electronic phenomena.³⁸⁻⁴² Among them, the intercalation of electron-donating atoms has been an effective method to modulate intrinsic electronic properties, such as shifting the fermi level to higher or lower energy⁴³, changing band gap characteristics⁴⁴⁻⁴⁶ and inducing phase transitions.^{47,48} Morosan *et al.* reported that the phase transition arising at Fermi level in Cu-intercalated TiSe_2 could give rise to the new superconducting state in TiSe_2 .⁴⁹ Topological phase transition occurred in $\text{BiTl}(\text{S}_{1-\delta}\text{Se}_\delta)_2$ and Bi_2Se_3 , as well as superconductivity in $\text{Cu}_x\text{ZrTe}_{2-y}$ with different doping ratio of Se, Copthalocyanine and Cu atoms respectively.⁵⁰⁻⁵² Similarly, Tsipas *et al.* recently observed the semimetallic phase with massless Dirac Fermions is in ZrTe_2 .⁵³ The structure and electronic properties of the materials can be ascribes as a semiconductor or a semimetallic states with a small indirect or direct gap can be suppressed by intercalation or elemental doping.^{3, 16, 18-22, 31, 49} Likewise, the semiconductor to metal transition was witnessed MoTe_2 by strain or structural and

electronic phase transition by W substitution.⁵⁴ In principle, the states of quantum matter: charge density waves, insulators, and superconductors can be ascribed from the spectral energy gap with different bandgap structures.⁵⁵⁻⁵⁷ Therefore, the fundamental changes in the band structure can provide vital information for considering and controlling physical and electronic properties.⁵⁸

In this particular work, we synthesized Cu-intercalated zirconium diselenide (ZrSe_2) single crystals via chemical vapor transport technique (CVT), and investigated the change in electronic properties in comparison with pristine ZrSe_2 by combining synchrotron-based Angle Resolved Photoemission Spectroscopy (ARPES) with first-principles density functional theory (DFT) calculations. With the intercalation of Cu atoms, more electrons fill the bottom of conduction bands of ZrSe_2 , which change the electronic structure from semiconducting to metallic characters. Notably, this presented intercalation approach does not induce notable changes of crystal structure and overall band dispersions, indicating its high potentials for clean electron doping systems.

A high quality ZrSe_2 and Cu intercalated ZrSe_2 (Cu_xZrSe_2 , $x = 0.07$, x value was determined by ICP) single crystals were synthesized via an improved CVT method. The experimental detail of CVT synthesis is provided in the experimental part of the paper. The single crystal X-ray diffraction (XRD) patterns recorded on ZrSe_2 and $\text{Cu}_{0.07}\text{ZrSe}_2$ samples at room temperature are shown in **Fig. 1**. The (001), (002), (003) and (004) peaks indicate the high quality single crystals of both samples. The diffraction peaks emerged at the same angles in both ZrSe_2 and $\text{Cu}_{0.07}\text{ZrSe}_2$, with a small change in the c -lattice constant from 6.1889 Å to 6.2035 Å after Cu-intercalation along (001) plane calculated from XRD. Similarly, the peak intensities of $\text{Cu}_{0.07}\text{ZrSe}_2$ are enhanced, which is due to its increased crystallinity and other growth process. Highly crystalline large-sized single crystals of ZrSe_2 and $\text{Cu}_{0.07}\text{ZrSe}_2$ can be seen inside the XRD figure having a typical lateral size of ~0.8-1cm with silver grey colour and hexagonal shape respectively.

To investigate the chemical compositions and elemental ratio in the grown crystals, X-ray photoelectron spectroscopy (XPS) was performed. Typical XPS spectra of ZrSe₂ and Cu_{0.07}ZrSe₂ are shown in **Fig. 2**. For ZrSe₂, the obvious Zr 3d (Zr-3d_{5/2}, Zr-3d_{3/2}) peaks at 183.05 eV and 185 eV are displayed, along with clear Se 3d (Se-3d_{5/2}, Se-3d_{3/2}) peaks at 53.55 eV and 54.2 eV. These peak positions indicate the similar chemical bonding state for both ZrSe₂ and Cu_{0.07}ZrSe₂, with a small displacement of Zr-3d_{3/2} to lower energy, while donating electron to Se atoms and Se-3d to higher energy due to the emergence of electrons from Zr and Cu atoms in case of Cu_{0.07}ZrSe₂. Moreover, **Fig. 2(c)** shows Cu 2p (Cu-2p_{3/2} and Cu-2p_{1/2}) peaks at 932.2 eV and 952.2 eV. There is no satellite peak of Cu²⁺ in the obtained Cu_{0.07}ZrSe₂ crystals, instead Cu⁺¹ peak is visible. This can be ascribed to the electron donation from the intercalated Cu⁰ atoms to ZrSe₂ layers, resulting in Cu⁺¹ state that is consistent with previous Cu-substituted compounds.⁵⁹

In order to investigate the detailed local microstructure, compositions and topographical information with an atomic arrangement, we employed a high resolution scanning transmission electron microscopy (STEM) on Cu_{0.07}ZrSe₂. **Fig. 3(a)** is typical Z-contrast high resolution image recorded through STEM, showing the surface topography of atoms. It reveals a regular structure with perfect hexagonal atomic arrangement as indicated by inset red line frame. The microstructure of Cu_{0.07}ZrSe₂ is similar to that of pristine ZrSe₂ (see HRTEM image in **Fig. S1**). **Fig. 3(b)** shows a sketch of elemental configuration of ZrSe₂ with a hexagonal arrangements. The layered structure (Zr-Se) is indicating the hexagonal structure of Cu_{0.07}ZrSe₂ having two planes of Se atoms separated by Zr atoms with Cu ions randomly intercalated between the layers. Similarly, **Fig. 3(c)** shows a uniform structure of different layers with a d-spacing of about 2.29 Å that corresponds to (002) and Zr-Zr atom bond length of 1.73 Å corresponding to (003) lattice plane. From the d-spacing, it has been observed that Cu_{0.07}ZrSe₂ have the same layers spacing as that of ZrSe₂, with

a negligible enlargement. The Z-contrast intensity of lattices corresponds to the inset side view profile of the chemical structure in **Fig. 3(c)**. The crystal orientation and diffraction pattern were measured by selected-area electron diffraction (SAED). The SAED pattern of $\text{Cu}_{0.07}\text{ZrSe}_2$ in **Fig. 3(d)** contains a set of diffraction spots along the rotational direction of superlattice (002) and (110) zone axes of a hexagon, which is consistent with XRD results and STEM images. The diffraction spots corresponding to the $\text{Cu}_{0.07}\text{ZrSe}_2$ are different from pristine sample in terms of the intensities and rational direction (see inset SAED image in **Fig. S1**). The diffraction spots of $\text{Cu}_{0.07}\text{ZrSe}_2$ are much brighter without 60° rotation in comparison with the lower brightness and have 60° rotation of diffraction spots in ZrSe_2 . The elemental mapping images in **Fig. 3(e)** further confirm the homogeneous elemental distributions of Zr, Se and Cu atoms in the single crystal $\text{Cu}_{0.07}\text{ZrSe}_2$. Besides, that the energy dispersive X-ray spectroscopy (EDS) recorded for the samples also shows the existence adequate amount of Cu, Zr and Se elements in the single crystal (see **Fig. S2**, in supporting information). The stoichiometric ratio of Cu atoms is about 7wt%, as determined by inductively coupled plasma mass spectroscopy (ICP-MS) measurements as shown in **Table S1**. Combining the STEM analysis with XPS results, we can suggest that a small amount of Cu atoms have been randomly distributed into ZrSe_2 interlayers without any lattice changes.

To study the electronic properties, we performed DFT calculations to explore the band structures of pristine and Cu-intercalated ZrSe_2 single crystals. The computational details are given in the experimental section (supporting information). The structural model of bulk ZrSe_2 for calculations with a same hexagonal Brillouin zone (BZ) for both ZrSe_2 and Cu-intercalated ZrSe_2 of high-symmetry points is shown in **Fig. 4(a, b)** respectively. The calculated band structure results for ZrSe_2 are depicted in **Fig. 4(c)**. The band structure of ZrSe_2 shows that the valance band maximum (VBM) appears at Γ point, which is mainly attributed by the p-orbitals of Se atoms. In

contrast, the conduction band minima (CBM) appeared at 0.29 eV above the Fermi level at L point, showing a semiconductor with an indirect band gap of 0.71 eV. After the intercalation of Cu atoms, the emergence of conduction band which crosses over the Fermi level at M/L points, indicates the excess electron doping donated from Cu, changing the system from semiconductor to metallic state as shown from the red line in **Fig. 4(c)**, adopted from the calculated band structures of Cu-intercalated ZrSe₂ (**Fig. S3(c)**). The donated electron from the Cu 4s shell can make a stable closed-shell Cu⁺ resulting in an increased charge distribution within ZrSe₂ layers. Notably, the intercalation of copper atom merely provides a change of carrier concentration without modifying band dispersions and the structural integrity of ZrSe₂ layers. From **Fig. 4(c)** we further confirmed that the emerging CB is composed of Zr-d_{yz} and Zr-d_{z2} at M and L points, while the VB composed of Se-p_z and Se-p_y of high symmetry Γ point, (as we can see that from **Fig. S3(c)**). The Cu-p and Cu-d can only contribute in deeper energy (**Fig. S3(d)**), which can donate electrons to lift the Fermi level above the bottom of conduction band that is mainly composed of Zr-d orbitals. Based on band calculations, one can notice that a variation of doping can induce either hole or electron-type carriers, as dominated by different orbital characters from distinct elements as shown from **Fig. 4(c)**. This can potentially provide additional freedom to manipulate electronic properties of charge carriers.

We further investigated the band structures through angle resolved photoemission spectroscopy (ARPES). According to previous ARPES investigation of ZrSe₂⁶⁰, we can determine the k_z value accurately. Using the equation $k_{\perp} = \sqrt{(2m/\hbar^2) (E_{kin} \cos^2 \theta + |V_0|)}$ (where k_{\perp} is the momentum value along k_z , m is the electron mass, E_{kin} is the kinetic energy of the photoelectron,

V_0 is the inner potential), in combination with the data in⁶⁰, we can determine $V_0 = 10.9$ eV, which gives 30 eV and 42 eV photon energies for Γ and A, respectively.

Fig. 5 shows the ARPES intensity of ZrSe_2 and $\text{Cu}_{0.07}\text{ZrSe}_2$ at various binding energies, measured in the first Brillouin zone at $T=26$ K. There is no spectral weight at the Fermi level in ZrSe_2 (**Fig. 5(a₁)**), where one can notice electronic states around M at the Fermi level in $\text{Cu}_{0.07}\text{ZrSe}_2$ (**Fig. 5(b₁)**), indicating that electrons are doped into the parent electronic system of ZrSe_2 after Cu intercalation. As shown in band calculations, these electronic states come from the bottom of conduction bands. While going into deeper binding energies, the spectral weight distributions are very similar in both ZrSe_2 (**Fig. 5(a₂₋₅)**) and $\text{Cu}_{0.07}\text{ZrSe}_2$ (**Fig. 5(b₂₋₅)**), showing a symmetry consistent with the lattice structure of ZrSe_2 , though the pocket size changes slightly due to different electron doping level.

By comparing the band structure of Cu intercalated ZrSe_2 to that of pristine ZrSe_2 , we can reveal how the electronic structures vary after the intercalation. **Figs. 6(a, b)** show the E vs k dispersions of ZrSe_2 and $\text{Cu}_{0.07}\text{ZrSe}_2$ along the $\Gamma \rightarrow \text{M}$ direction, and **Figs. 6(c, d)** show data taken along the $\text{A} \rightarrow \text{L}$ direction. The pristine ZrSe_2 is a semiconductor, and our ARPES in **Figs. 6(a, c)** show that the Fermi level is within the band gap, and the top of the valence band is located at around -0.87 eV in binding energy. After the intercalation of Cu atoms, the band structures move to deeper binding energy by 70 meV, and the Fermi level cuts across the bottom of conduction bands around the zone boundary (see **Figs. 6(b, d)**), which gives rise to the electron pockets around M shown in **Fig. 5(b₁)**. Such a shift of Fermi level indicates that Cu atoms donate electrons into the pristine ZrSe_2 electronic systems, and changes it from a semiconductor to a conductor. There are no evident changes in the band dispersions with the Cu intercalation, suggesting that the electron correlation and the dimensionality of individual bands remain the same as pristine ZrSe_2 .

In **Figs. 6(e, f)**, one can notice that the bottom of the conduction band is deeper at L, and this difference arises from the 3D characteristics of the conduction bands. The introduction of Cu induces an electron doping without the change of overall band dispersions, and this provides an opportunity to study the gap structure in the pristine ZrSe₂. In **Figs. 6(b, d)**, we can clearly see that there is an indirect gap. The top of the valence band is at -0.94 eV, the bottom of conduction band is at -0.17 eV in **Fig. 6(f)**, and these values yield an indirect band gap of 0.77 eV, which is highly consistent with the calculated band gap of 0.71 eV. The red lines in **Figs. 6(e, f)** show the calculated band structures adopted from **Fig. S3(c)** consist of Zr-d_{yz} and Zr-d_{z2} orbitals, which are well matched with the experiment estimation data. In addition, both of **Figs. 6(b, d)** shows non-dispersive spectral weight at around -0.5 eV, which is absent in the pristine ZrSe₂. This feature can be attributed to some localized electronic states of Cu atoms intercalated in between the ZrSe₂ layers.

Furthermore, electrical properties were also investigated to confirm the metallic character of the as-synthesized Cu_{0.07}ZrSe₂ in comparison with the semiconducting ZrSe₂, the field effect transistors (FETs) were fabricated on ZrSe₂ and Cu_{0.07}ZrSe₂ multilayers (in **Fig. 7a**) using Au/Ti as contact electrodes on SiO₂/Si substrate. **Fig. 7(b)** shows the channel length of the FETs with around 10 μm. **Fig. 7(c, d)** represents the output I_{ds}-V_{ds} curves of the FET devices based on ZrSe₂ and Cu_{0.07}ZrSe₂. The forward and backward transport behaviour of ZrSe₂ displays gate tuneable I_{ds}-V_{ds} properties under V_{gs}=0V, while the linear curve of the Cu_{0.07}ZrSe₂ shows metallic behaviour. In **Fig. 7(d)**, the slope of I_{ds}-V_{ds} curve of ZrSe₂ decreases with decreasing gate voltage from 30 to -30 V, showing n-type transport behaviour (the magnified image from V_{ds} = 0-0.4V as shown in **Fig. S4** with clear gate tuneable characteristics), whereas the linear I_{ds}-V_{ds} curves of

$\text{Cu}_{0.07}\text{ZrSe}_2$ for all input gate voltages indicated Ohmic contact like behaviour between the metal electrodes with no tuneable character, strongly confirming the metallic behaviour.

In summary, we have controllably intercalated Cu atoms into layered ZrSe_2 single crystal via an improved CVT method, and comparatively studied the changes of microstructure and electronic structure of the ZrSe_2 and $\text{Cu}_{0.07}\text{ZrSe}_2$ by using first-principles calculations and ARPES. Both our DFT calculations and experimental results clearly revealed the presence of the metallic state in $\text{Cu}_{0.07}\text{ZrSe}_2$ with an indirect bandgap nature that is very different from the semiconducting character in ZrSe_2 . Similarly, the FET results further confirmed the semiconductor to metallic phase transition in ZrSe_2 after the intercalation of Cu atoms. These results are highlighting the significance of atomic intercalation-induced electron doping in 2D layered materials, which might be a vital trend for future valleytronic and electronics applications.

ASSOCIATED CONTENT

Supporting Information. Experimental section, CVT growth procedure, ARPES measurement, theoretical calculations, additional characterization and results.

AUTHOR INFORMATION

Corresponding Author

*E-mail: zsun@ustc.edu.cn (Z.S.); song2012@ustc.edu.cn (L.S.)

Author Contributions

⁺Z.M. and K.M. contributed equally to this work. L.S. and Z.S. supervised the project and designed the experiments. Z.M. carried out most of the experiments and analyzed the data. K.M. and Z.S. performed ARPES measurement and analysis. H.L. and X.W. performed the DFT calculations. C.W., Z.U.R. and M.H. partially contributed to experimental characterizations. Z.M., K.J.M., Z.S., X.W. and L.S. analyzed the data and co-wrote the paper. All authors discussed the results and commented on the manuscript.

ACKNOWLEDGMENT

The authors acknowledge the financial support from the MOST (2017YFA0303500, 2017YFA0402901, 2016YFA0200602, 2014CB848900, 2014CB921102), NSFC (U1532112, U1532136, 11574280, 11190022), CAS Key Research Program of Frontier Sciences (QYZDB-SSW-SLH018) and CAS Interdisciplinary Innovation Team. Z.M. acknowledges the CSC

(Chinese Scholarship Council) Program. L.S. acknowledges the support from Key Laboratory of Advanced Energy Materials Chemistry (Ministry of Education) Nankai University, and Key Laboratory of the Ministry of Education for Advanced Catalysis Materials and Zhejiang Key Laboratory for Reactive Chemistry on Solid Surfaces (Zhejiang Normal University). We thanks the Hefei Synchrotron Radiation Facility (Angle Resolved Photoemission Spectroscopy and Photoemission Endstations, NSRL), and the USTC Center for Micro and Nanoscale Research and Fabrication for helps in characterizations.

Notes

The authors declare no competing financial interests

REFERENCES

- (1) Balendhran, S.; Walia, S.; Nili, H.; Ou, J. Z.; Zhuiykov, S.; Kaner, R. B.; Sriram, S.; Bhaskaran, M.; Kalantar-zadeh, K., Two-dimensional molybdenum trioxide and dichalcogenides. *Adv. Funct. Mater.* **2013**, *23* (32), 3952-3970.
- (2) Butler, S. Z.; Hollen, S. M.; Cao, L.; Cui, Y.; Gupta, J. A.; Gutiérrez, H. R.; Heinz, T. F.; Hong, S. S.; Huang, J.; Ismach, A. F., Progress, challenges, and opportunities in two-dimensional materials beyond graphene. *ACS Nano* 2013, *7* (4), 2898-2926.
- (3) Tan, C.; Zhang, H., Two-dimensional transition metal dichalcogenide nanosheet-based composites. *Chem. Soc. Rev.* **2015**, *44* (9), 2713-2731.
- (4) Xia, F.; Wang, H.; Xiao, D.; Dubey, M.; Ramasubramaniam, A., Two-dimensional material nanophotonics. *Nat. Phot.* **2014**, *8* (12), 899-907.
- (5) Wang, X.; Huang, L.; Jiang, X.-W.; Li, Y.; Wei, Z.; Li, J., Large scale ZrS₂ atomically thin layers. *J. Mater. Chem. C* **2016**, *4* (15), 3143-3148.
- (6) Zhang, M.; Zhu, Y.; Wang, X.; Feng, Q.; Qiao, S.; Wen, W.; Chen, Y.; Cui, M.; Zhang, J.; Cai, C., Controlled synthesis of ZrS₂ monolayer and few layers on hexagonal boron nitride. *Journal of the Amer. Chem. Soc.* **2015**, *137* (22), 7051-7054.
- (7) Bhimanapati, Ganesh R., et al. "Recent advances in two-dimensional materials beyond graphene. *ACS Nano* **2015**, *9*, 11509.
- (8) Splendiani, A.; Sun, L.; Zhang, Y.; Li, T.; Kim, J.; Chim, C.-Y.; Galli, G.; Wang, F., Emerging photoluminescence in monolayer MoS₂. *Nano letters* **2010**, *10* (4), 1271-1275.
- (9) Kumar, A.; Ahluwalia, P., Electronic structure of transition metal dichalcogenides monolayers

1H-MX₂ (M= Mo, W; X= S, Se, Te) from ab-initio theory: new direct band gap semiconductors. *EPJ B* **2012**, 85 (6), 186.

- (10) Ellis, J. K.; Lucero, M. J.; Scuseria, G. E., The indirect to direct band gap transition in multilayered MoS₂ as predicted by screened hybrid density functional theory. *Appl. Phys. Lett.* **2011**, 99 (26), 261908.
- (11) Zhang, Y.; Chang, T.-R.; Zhou, B.; Cui, Y.-T.; Yan, H.; Liu, Z.; Schmitt, F.; Lee, J.; Moore, R.; Chen, Y., Direct observation of the transition from indirect to direct bandgap in atomically thin epitaxial MoSe₂. *Nat. Nanotech.* **2014**, 9 (2), 111-115.
- (12) Jin, W.; Yeh, P.-C.; Zaki, N.; Zhang, D.; Sadowski, J. T.; Al-Mahboob, A.; van Der Zande, A. M.; Chenet, D. A.; Dadap, J. I.; Herman, I. P., Direct measurement of the thickness-dependent electronic band structure of MoS₂ using angle-resolved photoemission spectroscopy. *Phys. Rev. Lett.* **2013**, 111 (10), 106801.
- (13) Roldán, R.; Silva-Guillén, J. A.; López-Sancho, M. P.; Guinea, F.; Cappelluti, E.; Ordejón, P., Electronic properties of single-layer and multilayer transition metal dichalcogenides MX₂ (M= Mo, W and X= S, Se). *Adp* **2014**, 526 (9-10), 347-357.
- (14) Zhu, Z.; Cheng, Y.; Schwingenschlögl, U., Giant spin-orbit-induced spin splitting in two-dimensional transition-metal dichalcogenide semiconductors. *Phys. Rev. B* **2011**, 84 (15), 153402.
- (15) Sun, L.; Yan, J.; Zhan, D.; Liu, L.; Hu, H.; Li, H.; Tay, B. K.; Kuo, J.-L.; Huang, C.-C.; Hewak, D. W., Spin-orbit splitting in single-layer MoS₂ revealed by triply resonant Raman scattering. *Phys. Rev. Lett.* **2013**, 111 (12), 126801.

- (16) Alidoust, N.; Bian, G.; Xu, S.-Y.; Sankar, R.; Neupane, M.; Liu, C.; Belopolski, I.; Qu, D.-X.; Denlinger, J. D.; Chou, F.-C., Observation of monolayer valence band spin-orbit effect and induced quantum well states in MoX₂. *Nat. commun.* **2014**, *5*, 4673.
- (17) Miwa, J. A.; Ulstrup, S.; Sørensen, S. G.; Dendzik, M.; Čabo, A. G.; Bianchi, M.; Lauritsen, J. V.; Hofmann, P., Electronic Structure of Epitaxial Single-Layer MoS₂. *Phys. Rev. Lett.* **2015**, *114* (4), 046802.
- (18) Riley, J. M.; Mazzola, F.; Dendzik, M.; Michiardi, M.; Takayama, T.; Bawden, L.; Granerød, C.; Leandersson, M.; Balasubramanian, T.; Hoesch, M., Direct observation of spin-polarized bulk bands in an inversion-symmetric semiconductor. *Nat. Phys.* **2014**, *10* (11), 835-839.
- (19) Mak, K. F.; He, K.; Shan, J.; Heinz, T. F., Control of valley polarization in monolayer MoS₂ by optical helicity. *Nat. Nanotech.* **2012**, *7* (8), 494-498.
- (20) Xiao, D.; Liu, G.-B.; Feng, W.; Xu, X.; Yao, W., Coupled spin and valley physics in monolayers of MoS₂ and other group-VI dichalcogenides. *Phys. Rev. Lett.* **2012**, *108* (19), 196802.
- (21) Zeng, H.; Dai, J.; Yao, W.; Xiao, D.; Cui, X., Valley polarization in MoS₂ monolayers by optical pumping. *Nat. Nanotech.* **2012**, *7* (8), 490-493.
- (22) Yu, H.; Cui, X.; Xu, X.; Yao, W., Valley excitons in two-dimensional semiconductors. *Nat. Sci. Rev.* **2015**, *2* (1), 57-70.
- (23) Cheiwchanchamnangij, T.; Lambrecht, W. R., Quasiparticle band structure calculation of monolayer, bilayer, and bulk MoS₂. *Phys. Rev. B* **2012**, *85* (20), 205302.

- (24) Komsa, H.-P.; Krasheninnikov, A. V., Effects of confinement and environment on the electronic structure and exciton binding energy of MoS₂ from first principles. *Phys. Rev. B* **2012**, *86* (24), 241201.
- (25) Ugeda, M. M.; Bradley, A. J.; Shi, S.-F.; Felipe, H.; Zhang, Y.; Qiu, D. Y.; Ruan, W.; Mo, S.-K.; Hussain, Z.; Shen, Z.-X., Giant bandgap renormalization and excitonic effects in a monolayer transition metal dichalcogenide semiconductor. *Nat. Mater.* **2014**, *13* (12), 1091-1095.
- (26) Qiu, D. Y.; Felipe, H.; Louie, S. G., Optical spectrum of MoS₂: many-body effects and diversity of exciton states. *Phys. Rev. Lett.* **2013**, *111* (21), 216805.
- (27) Rybkin, A. G.; Rybkina, A. A.; Otrokov, M. M.; Vilkov, O. Y.; Klimovskikh, I. I.; Petukhov, A. E.; Filianina, M. V.; Voroshnin, V. Y.; Rusinov, I. P.; Ernst, A.; Arnau, A., Magneto-spin-orbit graphene: interplay between exchange and spin-orbit couplings. *Nano letters* **2018**.
- (28) Späh, R.; Elrod, U.; Lux-Steiner, M.; Bucher, E.; Wagner, S., PN junctions in tungsten diselenide. *Appl. Phys. Lett.* **1983**, *43* (1), 79-81.
- (29) Podzorov, V.; Gershenson, M.; Kloc, C.; Zeis, R.; Bucher, E., High-mobility field-effect transistors based on transition metal dichalcogenides. *Appl. Phys. Lett.* **2004**, *84* (17), 3301-3303.
- (30) Gan, W.; Han, N.; Yang, C.; Wu, P.; Liu, Q.; Zhu, W.; Chen, S.; Wu, C.; Habib, M.; Sang, Y., A Ternary Alloy Substrate to Synthesize Monolayer Graphene with Liquid Carbon

Precursor. *ACS Nano* **2017**, *11* (2), 1371-1379.

- (31) Koenig, S. P.; Doganov, R. A.; Seixas, L.; Carvalho, A.; Tan, J. Y.; Watanabe, K.; Taniguchi, T.; Yakovlev, N.; Castro Neto, A. H.; Özyilmaz, B., Electron doping of ultrathin black phosphorus with Cu Adatoms. *Nano Lett.* **2016**, *16* (4), 2145-2151.
- (32) Lee, P.; Said, G.; Davis, R.; Lim, T., On the optical properties of some layer compounds. *J. Phys. Chem. Solids* **1969**, *30* (12), 2719-2729.
- (33) Britnell, L.; Ribeiro, R.; Eckmann, A.; Jalil, R.; Belle, B.; Mishchenko, A.; Kim, Y.-J.; Gorbachev, R.; Georgiou, T.; Morozov, S., Strong light-matter interactions in heterostructures of atomically thin films. *Science* **2013**, *340* (6138), 1311-1314.
- (34) Shi, S.-F.; Wang, F., Two-dimensional materials: Atomically thin pn junctions. *Nat. Nanotech.* **2014**, *9* (9), 664-665.
- (35) Niu, T.; Li, A., From two-dimensional materials to heterostructures. *Prog. Surf. Sci.* **2015**, *90* (1), 21-45.
- (36) Huang, C.; Wu, S.; Sanchez, A. M.; Peters, J. J.; Beanland, R.; Ross, J. S.; Rivera, P.; Yao, W.; Cobden, D. H.; Xu, X., Lateral heterojunctions within monolayer MoSe₂-WSe₂ semiconductors. *Nat. Mater.* **2014**, *13* (12), 1096-1101.
- (37) Kane, C. L.; Mele, E. J., Quantum spin Hall effect in graphene. *Phys. Rev. Lett.* **2005**, *95* (22), 226801.
- (38) Lee, D. S.; Riedl, C.; Beringer, T.; Neto, A. C.; von Klitzing, K.; Starke, U.; Smet, J. H., Quantum Hall effect in twisted bilayer graphene *Phys. Rev. Lett.* **2011**, *107* (21), 216602.

- (39) Abanin, D.; Pesin, D., Interaction-induced topological insulator states in strained graphene. *Phys. Rev. Lett.* **2012**, *109* (6), 066802.
- (40) Bao, C.; Yao, W.; Wang, E.; Chen, C.; Avila, J.; Asensio, M.C.; Zhou, S., Stacking-dependent electronic structure of trilayer graphene resolved by nanospot angle-resolved photoemission spectroscopy. *Nano letters* **2017**, *17*(3), 1564-1568.
- (41) Han, W.; Kawakami, R. K.; Gmitra, M.; Fabian, J., Graphene spintronics. *Nat. Nanotech.* **2014**, *9* (10), 794-807.
- (42) Tributsch, H., Photo-intercalation: Possible application in solar energy devices. *Appl. Phys. A: Mater. Sci. & Processing* **1980**, *23* (1), 61-71.
- (43) Wang, Y.-L.; Xu, Y.; Jiang, Y.-P.; Liu, J.-W.; Chang, C.-Z.; Chen, M.; Li, Z.; Song, C.-L.; Wang, L.-L.; He, K., Structural defects and electronic properties of the Cu-doped topological insulator Bi₂Se₃. *Phys. Rev. B* **2011**, *84* (7), 075335.
- (44) Kang, M., Kim, B., Ryu, S.H., Jung, S.W., Kim, J., Moreschini, L., Jozwiak, C., Rotenberg, E., Bostwick, A. and Kim, K.S., 2017. Universal mechanism of band-gap engineering in transition-metal dichalcogenides. *Nano letters*, *17*(3), pp.1610-1615.
- (45) Ruppert, C.; Aslan, O.B.; Heinz, T.F., Optical properties and band gap of single-and few-layer MoTe₂ crystals. *Nano letters* **2014**, *14*(11), 6231-6236.
- (46) N. Nair, M.; Palacio, I.; Celis, A.; Zobelli, A.; Gloter, A.; Kubsky, S.; Turmaud, J.P.; Conrad, M.; Berger, C.; de Heer, W.; Conrad, E.H., Band gap opening induced by the structural periodicity in epitaxial graphene buffer layer. *Nano letters* **2017**, *17*(4), 2681-2689.
- (47) Zhao, J.; Ou, H.; Wu, G.; Xie, B.; Zhang, Y.; Shen, D.; Wei, J.; Yang, L.; Dong, J.; Arita, M., Evolution of the Electronic Structure of 1T-Cu_xTiSe₂. *Phys. Rev. Lett* **2007**, *99* (14), 146401.

- (48) Liu, Q.; Ishikawa, R.; Funada, S.; Ohki, T.; Ueno, K.; Shirai, H., Highly Efficient Solution-Processed Poly (3, 4-ethylenedio-xythiophene): Poly (styrenesulfonate)/Crystalline–Silicon Heterojunction Solar Cells with Improved Light-Induced Stability. *Adv. Energy Mater.* **2015**, *5* (17).
- (49) Morosan, E.; Zandbergen, H.; Dennis, B.; Bos, J.; Onose, Y.; Klimczuk, T.; Ramirez, A.P.; Ong, N.P. and Cava, R.J., Superconductivity in Cu_xTiSe_2 . *Nat. Phys.* **2006**, *2*, 544.
- (50) Xu, S.-Y.; Xia, Y.; Wray, L.; Jia, S.; Meier, F.; Dil, J.; Osterwalder, J.; Slomski, B.; Bansil, A.; Lin, H., Topological phase transition and texture inversion in a tunable topological insulator. *Science* **2011**, *332* (6029), 560-564.
- (51) Caputo, M.; Panighel, M.; Lisi, S.; Khalil, L.; Santo, G.D.; Papalazarou, E.; Hruban, A.; Konczykowski, M.; Krusin-Elbaum, L.; Aliev, Z.S.; Babanly, M.B.; Manipulating the topological interface by molecular adsorbates: adsorption of Co-phthalocyanine on Bi_2Se_3 . *Nano letters* **2016**, *16*(6), 3409-3414.
- (52) Machado, A. J. S.; Baptista, N. P.; de Lima, B. S.; Chaia, N.; Grant, T. W.; Corrêa, L. E.; Renosto, S.T.; Scaramussa, A.C.; Jardim, R.F.; Torikachvili, M.S. and Aguiar, J.A., Evidence for topological behavior in superconducting $\text{Cu}_x\text{ZrTe}_{2-y}$. *Phys. Rev. B* **2017**, *95*(14), 144505.
- (53) Tsipas, P.; Tsoutsou, D.; Fragkos, S.; Sant, R.; Alvarez, C.; Okuno, H.; Renaud, G.; Alcotte, R.; Baron, T. and Dimoulas, A., Massless Dirac Fermions in ZrTe_2 Semimetal Grown on InAs (111) by van der Waals Epitaxy. *ACS Nano* **2018**, Jan 9.
- (54) Song, S.; Keum, D.H.; Cho, S.; Perello, D.; Kim, Y. and Lee, Y.H., Room temperature semiconductor–metal transition of MoTe_2 thin films engineered by strain. *Nano letters* **2015**, *16*(1), 188-193.
- (55) Rhodes, D.; Chenet, D.A.; Janicek, B.E.; Nyby, C.; Lin, Y.; Jin, W.; Edelberg, D.;

- Mannebach, E.; Finney, N.; Antony, A. and Schiros, T., Engineering the structural and electronic phases of MoTe₂ through W substitution. *Nano Letters* **2017**, *17*(3), 1616-1622.
- (56) Hashimoto, M.; Vishik, I. M.; He, R.-H.; Devereaux, T. P.; Shen, Z.-X., Energy gaps in high-transition-temperature cuprate superconductors. *Nat. Phys.* **2014**, *10* (7), 483-495.
- (57) Chen, P.; Chan, Y.-H.; Fang, X.-Y.; Zhang, Y.; Chou, M.-Y.; Mo, S.-K.; Hussain, Z.; Fedorov, A.-V.; Chiang, T.-C., Charge density wave transition in single-layer titanium diselenide. *Nat. Commun.* **2015**, *6*, 8943.
- (58) Mo, S.-K., Angle-resolved photoemission spectroscopy for the study of two-dimensional materials. *Nano Convergence* **2017**, *4* (1), 6.
- (59) Kuang, M.; Li, T. T.; Chen, H.; Zhang, S. M.; Zhang, L. L.; Zhang, Y. X., Hierarchical Cu₂O/CuO/Co₃O₄ core-shell nanowires: synthesis and electrochemical properties. *Nanotechnology* **2015**, *26* (30), 304002.
- (60) Moustafa, M.; Ghafari, A.; Paulheim, A.; Janowitz, C.; Manzke, R., Spin orbit splitting in the valence bands of ZrS_xSe_{2-x}: Angle resolved photoemission and density functional theory. *J Electron Spectros Relat Phenomena* **2013**, *189*, 35-39.

FIGURES CAPTIONS

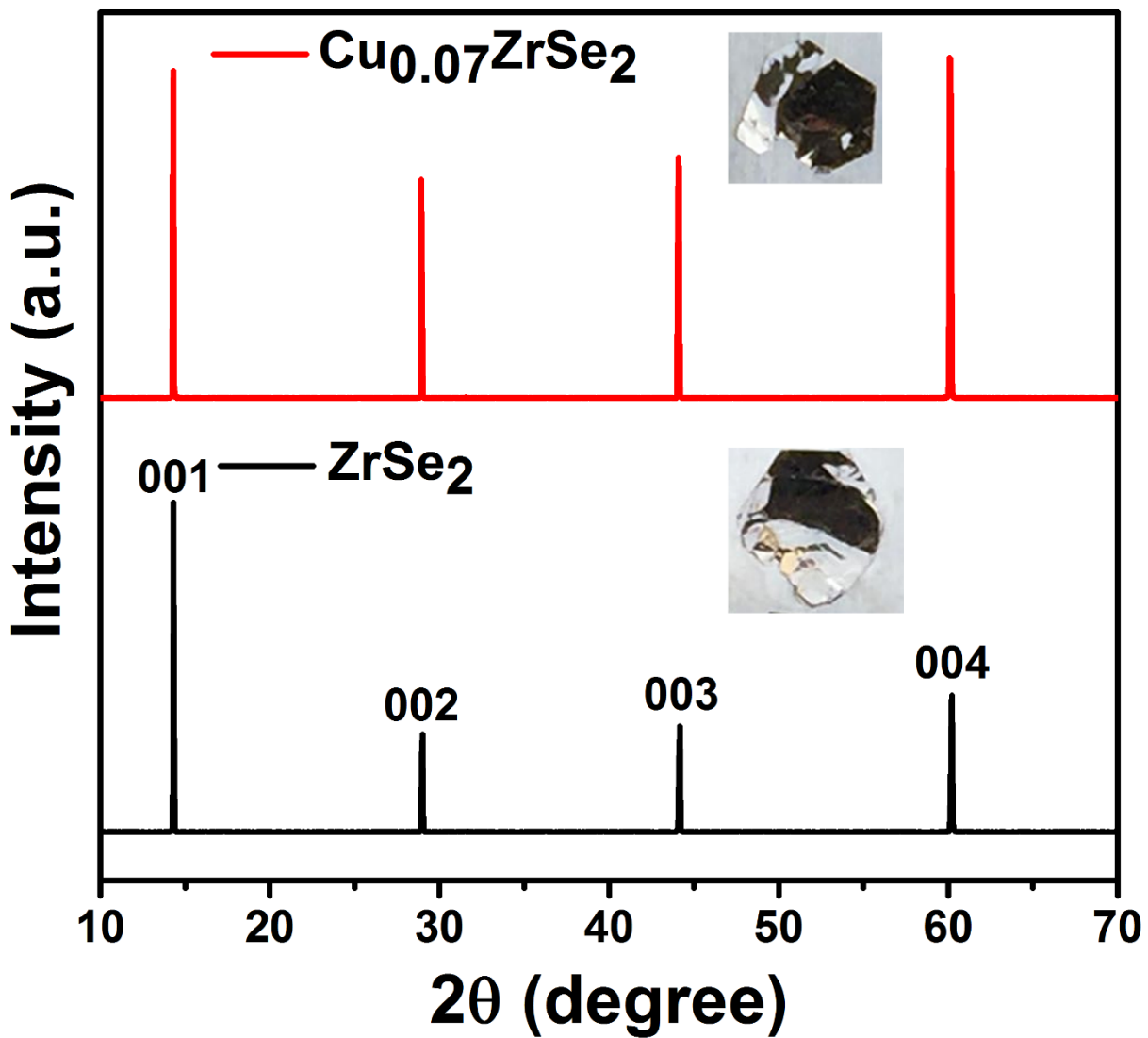


Figure 1. Single crystal XRD patterns of ZrSe_2 in comparison with $\text{Cu}_{0.07}\text{ZrSe}_2$ depicting the enhancement of peaks and negligible enlargement.

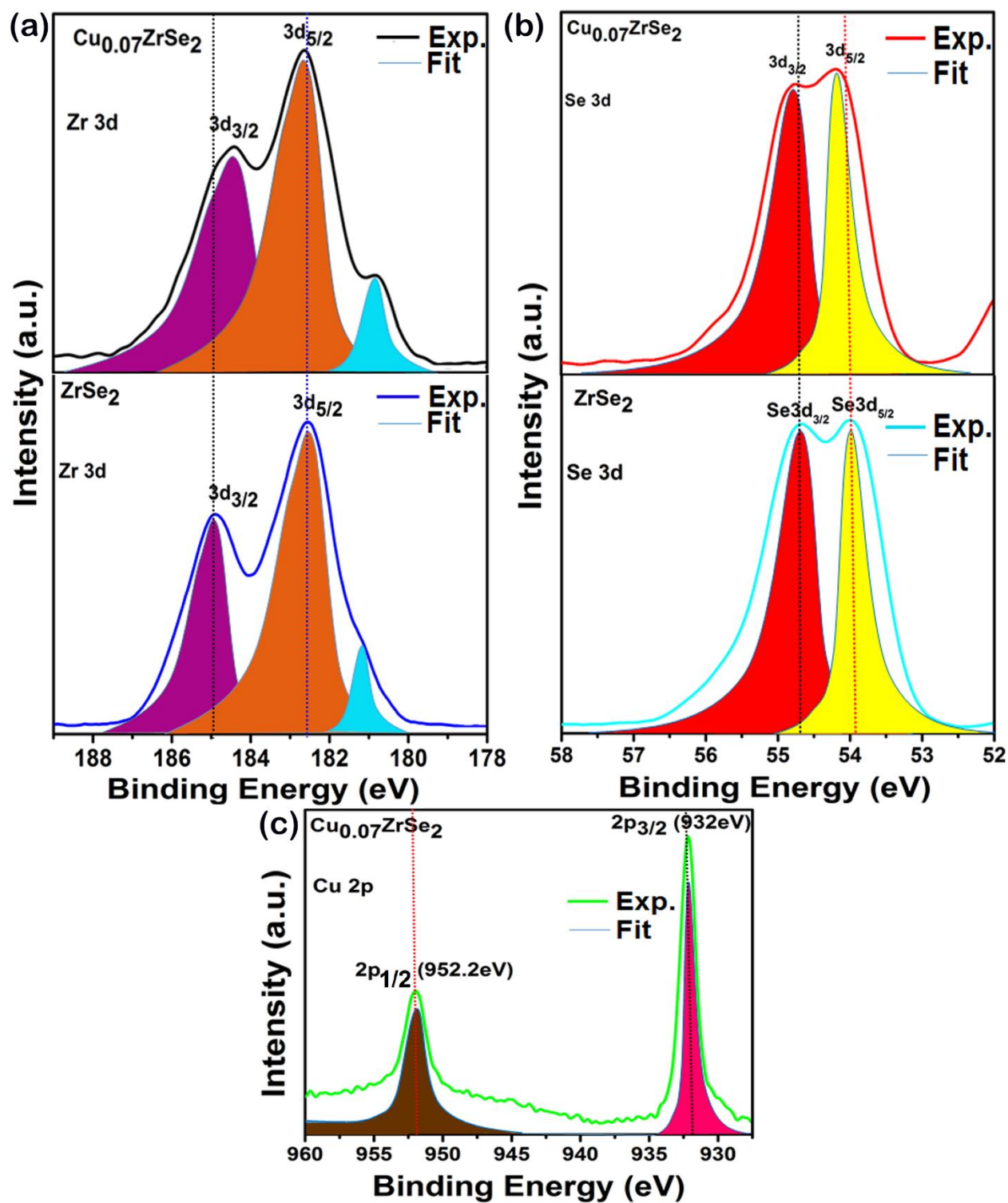


Figure 2. XPS analysis of as-synthesized ZrSe_2 and $\text{Cu}_{0.07}\text{ZrSe}_2$ single crystals. (a) Zirconium (Zr 3d). (b) Selenium, (Se 3d). (c) Copper (Cu 2p)

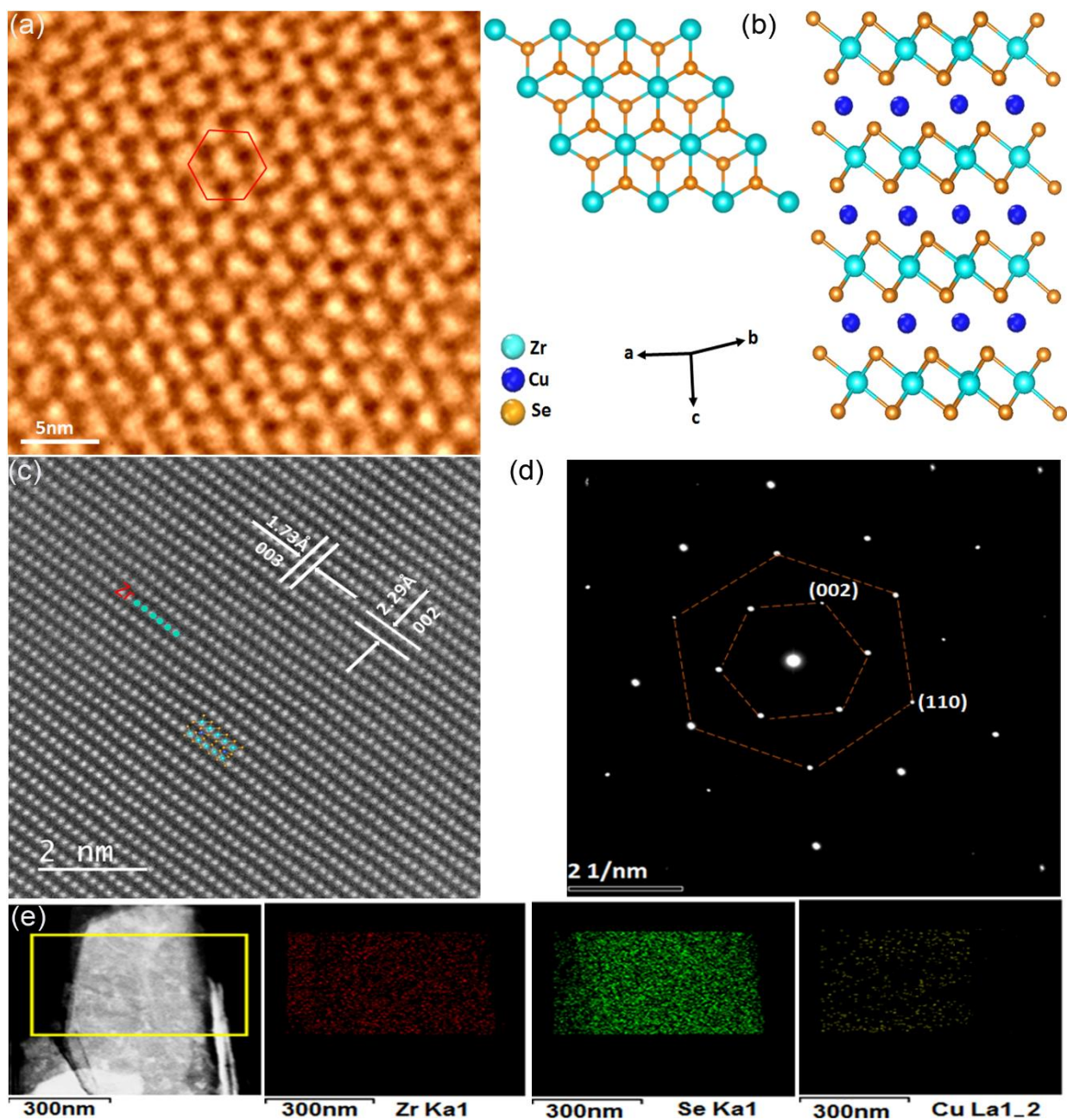


Figure 3. Microstructural characterizations of $\text{Cu}_{0.07}\text{ZrSe}_2$ single crystal through scanning transmission electron microscopy (STEM). (a) Typical STEM image with Z-contrast. (b) Structural configurations of bulk and side view of layered structure with Cu atom between the layers. (c) High resolution STEM image with specified layers identification and (d) SAED patterns of $\text{Cu}_{0.07}\text{ZrSe}_2$. (e) The elemental mapping image shows the uniform distribution of Zr, Se and Cu elements, respectively.

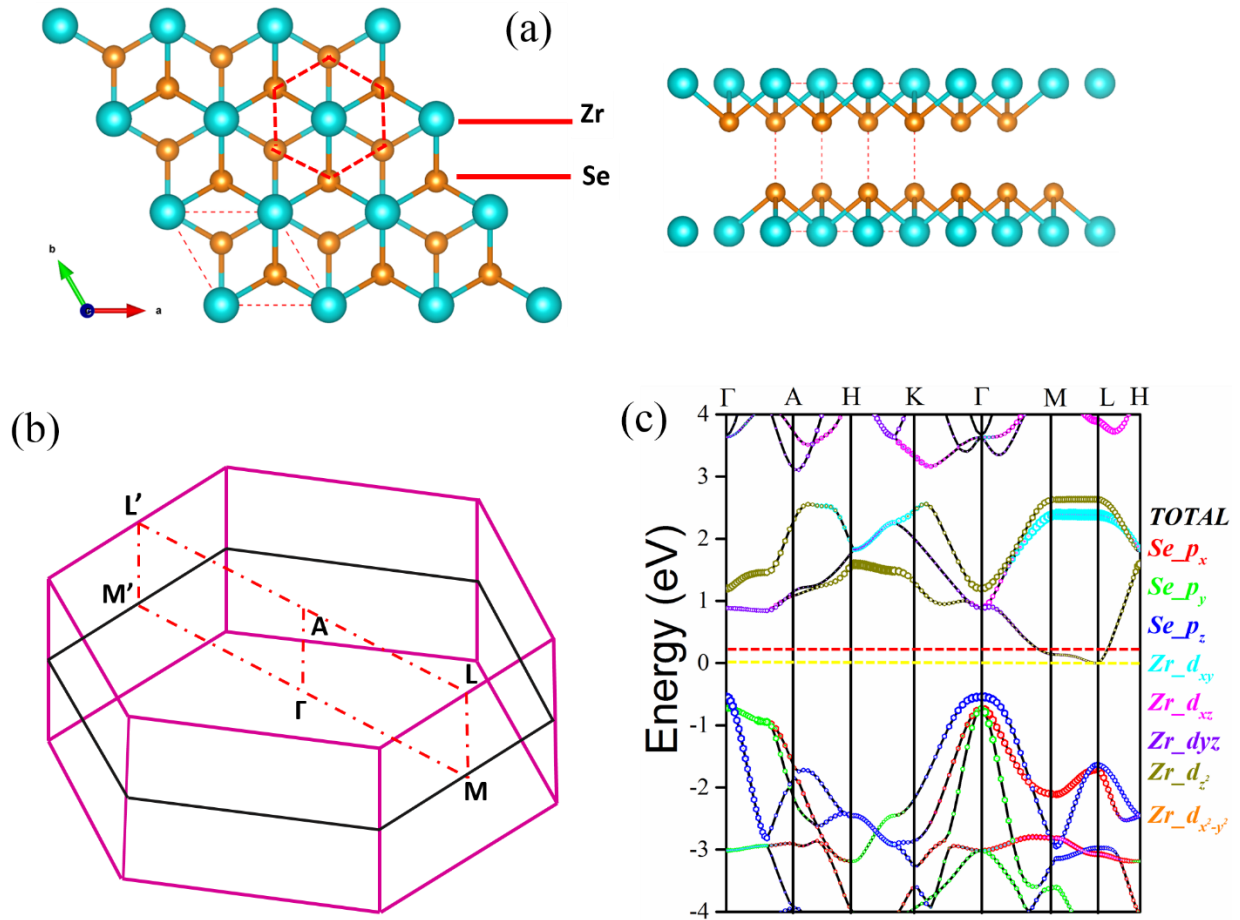


Figure 4. (a) Structural model of ZrSe_2 . (b) Hexagonal Brillouin zone (BZ). (c) DFT orbital decomposed band structure calculations of bulk ZrSe_2 along the high symmetry k-points. After the intercalation of Cu atoms, the emergence of conduction band at M points indicates excess electrons donation that can change the system from semiconductor to metallic state as shown from the dash red line.

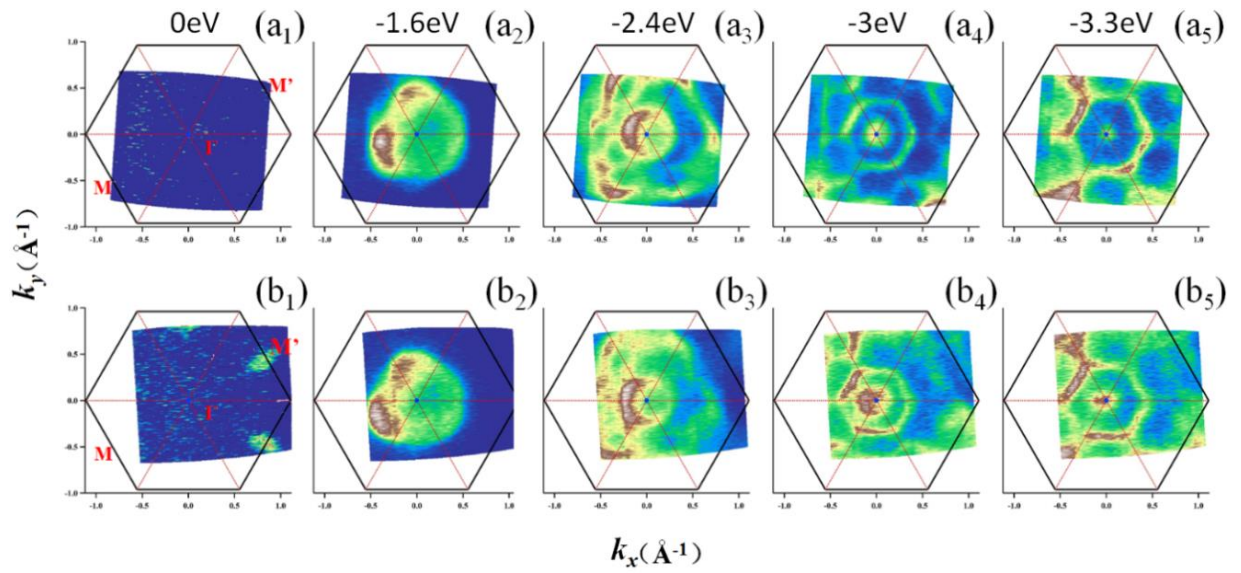


Figure 5. ARPES intensity of the pristine ZrSe_2 (upper panels, a_1 - a_5) and $\text{Cu}_{0.07}\text{ZrSe}_2$ (lower panels, b_1 - b_5) single crystals at various binding energies, taken with 30 eV photons. The black hexagonal boxes indicate the Brillouin zone.

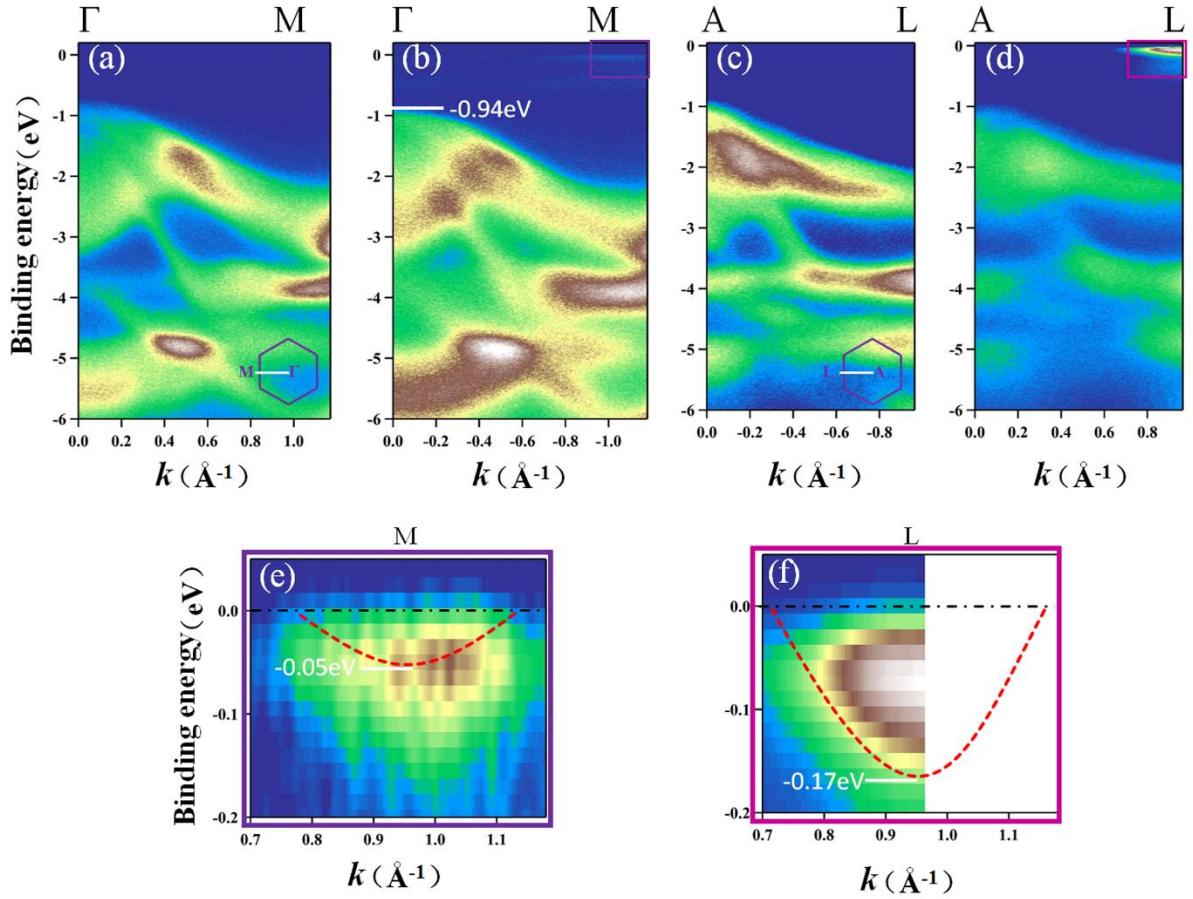


Figure 6. (a, b) The photoemission intensity plots along $\Gamma \rightarrow M$ direction of pristine $ZrSe_2$ and Cu intercalated $ZrSe_2$ single crystals, respectively. The data were taken using 30 eV photons. (c, d) The photoemission intensity plots along A \rightarrow L high direction of pristine $ZrSe_2$ and $Cu_{0.07}ZrSe_2$, respectively, taken using 42 eV photons. (e, f) The spectral weight of conduction bands around the zone boundary in panels b and d, respectively. The red dashed lines indicate the band dispersions from DFT calculations (adopted from Figure 4 (c)), consists of Zr d_{yz} and d_{z^2} orbitals.

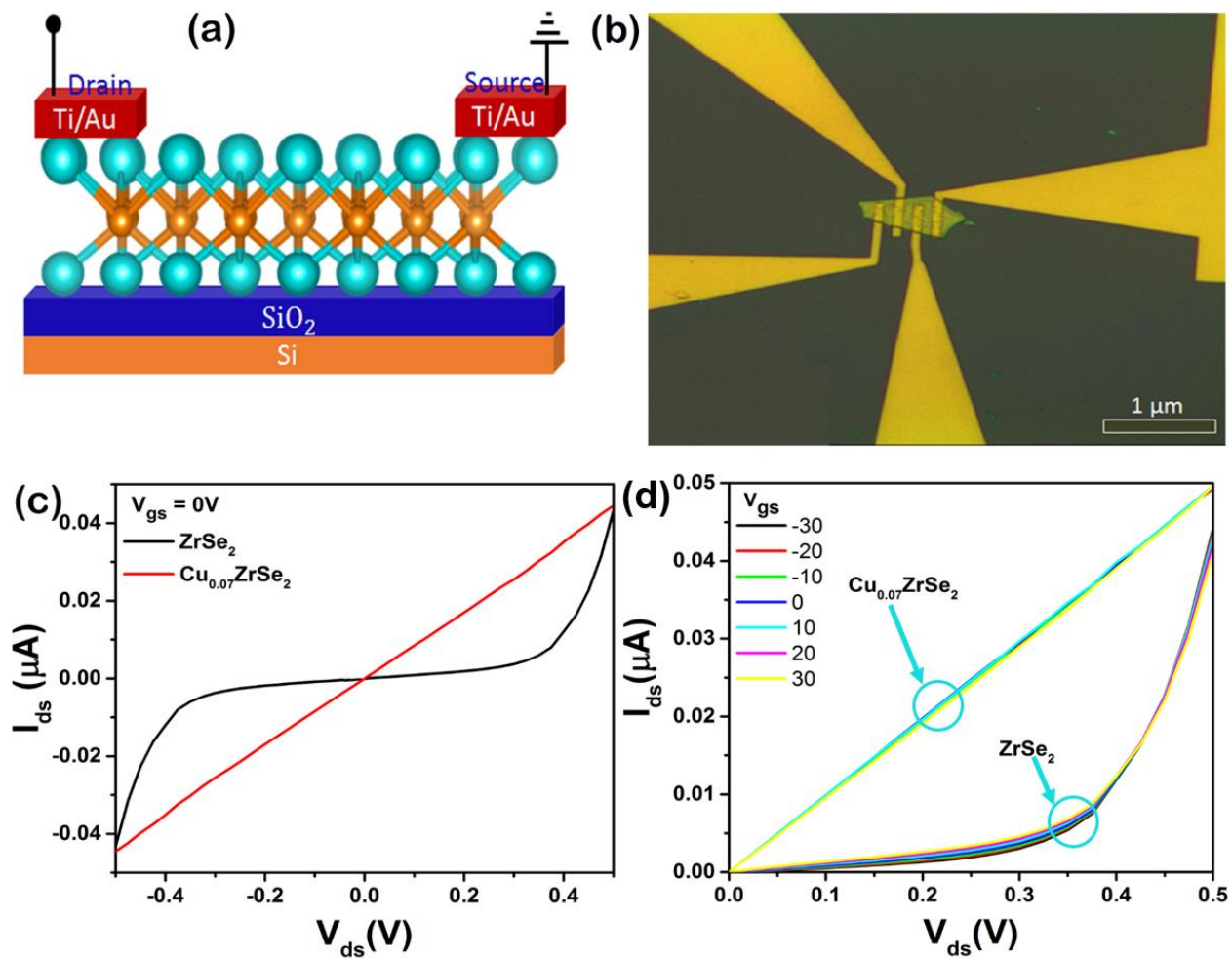


Figure 7. Typical FET device fabricated on ZrSe₂ and Cu_{0.07}ZrSe₂ exfoliated flakes. (a) Schematic of the device structure. (b) Optical image of the as-shaped nanodevice. The current-voltage curves at gate voltage = 0V showing (c) the forward and backward transport behavior indicate semiconducting and metallic behavior for ZrSe₂ and Cu_{0.07}ZrSe₂, respectively. (d) The output characteristics curves of ZrSe₂ and Cu_{0.07}ZrSe₂ at different gate voltages.

The table of contents:

Single crystal ZrSe₂ and atomic Cu-intercalated ZrSe₂ layered structures were synthesized in high crystalline quality by using chemical vapor transport method. Both theoretical DFT calculations and experimental ARPES results revealed a transition from semiconducting to metallic characteristics, indicating the emergence of conduction band dispersion at M/L point of Brillouin zone due to the electron doping of ZrSe₂ layers originated from additional atomic Cu intercalation.

TOC Figure:

